


 Cite this: *RSC Adv.*, 2021, **11**, 11329

Silver nanoparticle on zinc oxide array for label-free detection of opioids through surface-enhanced raman spectroscopy

 Michael Zhang,^{†a} Congran Jin,^{†a} Yuan Nie,^{†a} Yundong Ren,^a Nanjing Hao,^{†a} Zhe Xu,^{†a} Lin Dong^b and John X. J. Zhang^{*a}

Opioid abuse is a significant public health problem. Over two million Americans have some form of addiction to opioids; however, despite governmental programs established to treat overdoses and restrict opioid distribution, there are still few screening tools that are quantitative, portable and easy to use for high-throughput mapping and monitoring this ongoing crisis. In this paper, we demonstrated a plasmonic zinc oxide (ZnO) arrays-on-silicon sensor for the label-free detection of opioids through surface-enhanced Raman spectroscopy (SERS), and evaluated the chips' opioid sensing performance. Specifically, we tested our device with oxycodone, a potent and commonly abused opioid, dissolved in methanol and blood serum as a proof-of-concept study. Ag particles were *in situ* patterned onto the ZnO array to form the completed sensing platform. The resulting Ag@ZnO arrays were characterized using Scanning Electron Microscopy (SEM), Energy Dispersive X-ray Analysis (EDS), and element mapping. In addition, the enhanced electric field induced by the localized surface plasmonic resonance at the Ag particle decorated ZnO is simulated using COMSOL. Opioid-containing samples at varying concentrations, from 900 $\mu\text{g mL}^{-1}$ to 90 ng mL^{-1} were tested using SERS to characterize the chip's accuracy and sensitivity. We demonstrated that the sensor can reliably detect opioid concentrations as low as 90 ng mL^{-1} with great accuracy and sensitivity even spiked into blood serum. The chips could provide a cost-effective, high-throughput method for detecting opiate oxycodone, thereby providing a powerful tool to monitor and control the emerging public health threats.

Received 28th January 2021

Accepted 3rd March 2021

DOI: 10.1039/d1ra00760b

rsc.li/rsc-advances

1 Introduction

The opioid crisis has posed major challenges for communities across America and the world for decades. For example, oxycodone, one of the most abused opioids, caused an average of 5526 deaths every year from year 2011 to 2016.¹ Despite current attempts to cure the adverse impacts of opioid abuse and overdoses as they appear, there are still few tools available to map and understand this ongoing epidemic. For opioid substance detection, there are two existing commercially available techniques, namely the immunoassays and gas chromatography-mass spectrometry (GC-MS).^{2,3} The working mechanism of the immunoassay method is to utilize the change in enzyme activity when a specific antibody binds the drug, and the enzyme activity is measured using spectrophotometry. However, most immunoassays have a poor reaction to opiate substances like

oxycodone and oxymorphone and may lead to false-negative results.^{4,5} The GC-MS method works by first separating the sample mixture through heating and flow of gas, then the MS identifies the individual substance by measuring and comparing the mass of the molecule. This method provides more accurate results, but the technique is costly, requiring a time-consuming and laborious sample preparation procedure which can take up to 24 hours.⁴ In recent years, Surface-Enhanced Raman Spectroscopy (SERS) has become a popular method of detecting trace amounts of chemical compounds, especially drugs,^{6–15} due to its ability to enhance the Raman scattering signals of detection targets with high sensitivity, rapid detection time, and non-destructive analysis method.^{16,17} For example, Masterson *et al.*⁹ developed a flexible SERS patch with chemically functionalized Au triangular prisms for detecting highly potent drugs. However, a limitation of many current SERS based opioid detecting devices is that they have not been tested using real blood samples, which is an important step for verifying the device's performance in practical settings for detecting the drug use in people.^{6–8,10–12,14,15,18} In addition, these current SERS based sensor of opioid can only detect opioid with a concentration as low as several hundred nanograms per milliliter or even

^aThayer School of Engineering at Dartmouth College, Hanover, NH, USA. E-mail: john.zhang@dartmouth.edu

^bMechanical and Industrial Engineering, New Jersey Institute of Technology, Newark, NJ, USA

[†] Equal contribution.


higher. For example, while Shende *et al.*¹³ have tested the drugs in blood, their experimental detection limit is 500 ng mL⁻¹ which is too large for detecting trace amount. Another challenge in many SERS applications is the selection of a highly efficient plasmonic enhancement substance and the optimization of the detection substrate design. In particular, noble metals are usually the material of choice for SERS platforms due to their desirable plasmonic properties, which allows for enhancing Raman signals when stimulated electromagnetically *via* localized surface plasmon resonance (LSPR).¹⁹ Specifically, interactions between the electron clouds of nanoscale conductive particles and relatively larger electromagnetic waves result in regular oscillations of the particle's electrons, creating an evanescent conduction band in which the electromagnetic wave is trapped. This conduction band creates an amplification effect for many spectroscopic methods that measure a substrate's scattering properties, making it particularly useful in SERS applications.²⁰

Many of research of suitable LSPR materials for SERS has been centered around gold due to its relative biocompatibility.^{21–25} However, these advantages of gold come at the immensely higher production costs. Furthermore, Ag has higher electrical and thermal conductivity, making it a more efficient and cost-effective plasmonic material for use in spectroscopic enhancement, and as a result it has been widely used for SERS based measurement.^{19,26–39} Therefore, Ag is a superior surface-coated noble metal for SERS sensor platforms. Popular SERS sensor platform designs include the use of colloids nanospheres, nanorods and, or more complex 3D structures such as arrays, nanotrees, nanoflowers, or even butterfly-inspired structures.^{32,40–42} In particular, the category of novel 3D designs has become a topic of interest due to their ability to increase the platform surface area significantly, therefore allowing for a higher density of coated plasmonic materials. This allows for “hotspots” of plasmonic enhancement, enabling highly reproducible, sensitive, and specific molecular sensing. Zinc oxide (ZnO) has emerged as a popular platform synthesis material due to its biosafety, versatility and low-cost manufacturing. In addition, its excellent optoelectronic and electrochemical properties have enabled various sensing and biomedical engineering applications.^{43,44} ZnO array has been widely used to provide the platform for SERS-based sensing of various substances as it offers a higher reproducibility and stability,³⁵ larger surface-to-volume ratio²⁷ and a 3D platform.³⁹

In this study, we utilized a custom two-step hydrothermal growth and ultraviolet (UV) irradiation protocol to synthesize Ag particles decorated ZnO arrays on a silicon chip. These particles contribute to the local surface plasmonic effect and an increase in Ag SERS enhancement “hotspots”. This chip has superior testing capability which can measure a low oxycodone concentration of 90 ng mL⁻¹. The system of the Ag nanoparticles decorated ZnO array on a chip is the first of its kind that serve as a portable, cost-effective, timely, sensitive and highly specific SERS sensor for the detection of dissolved opioid substances at a low concentration which has the potential to be used in many healthcare applications in the drug abuse crisis.

2 Experimental

2.1 Materials and reagents

Zinc acetate ((CH₃CO₂)₂Zn, 99.99%), zinc nitrate hexahydrate (Zn(NO₃)₂·6H₂O, 98.0%), hexamethylenetetramine (C₆H₁₂N₄, HMTA, ≥99.0%), silver nitrate powder (AgNO₃, ≥99.0%) and 1 mg mL⁻¹ oxycodone solution (item id O-002-1ML) are purchased from Sigma Aldrich. Deionized (DI) water is from a Milli-Q water ultrapure water purification system. The silicon wafer ((1 0 0), single-side-polished) is purchased from Wafer University.

2.2 Chip fabrication

The fabrication process of the Ag particle decorated ZnO array chip is summarized as the following. First, a piece of Si wafer is cut into an approximately 2 cm by 2 cm square and is washed by deionized (DI) water and treated by oxygen plasma. Next, thermal treatment decomposes zinc acetate into ZnO nanocrystals as seeds on the Si substrate for the following synthesis of vertically aligned ZnO array. The vertically aligned ZnO array growth method is adapted from previously reported experiments.^{45,46} Specifically, the substrate is covered by a layer of 5 mM zinc acetate solution (in DI water) and then transferred into an oven at 180 °C for 40 min for thermal decomposition of the zinc acetate to create ZnO seeds on the substrate. Then, zinc nitrate hexahydrate (75 mM) and HMTA (50 mM) are added to 45 mL of DI water followed by sonication for 5 min to provide the hydrothermal growth solution. Then, the seeded substrate is then placed in the growth solution with the seeded side facing downward in a beaker which is covered by aluminum foil and placed in an oven for 3 hours at a temperature of 88 °C. This growth cycle with newly made growth solution is repeated 6 times to grow vertical ZnO wire of ~12 μm in height. Next, the chip is rinsed with DI water to remove ZnO residuals and dried in an oven at 50 °C. Lastly, UV irradiation method is employed to generate the Ag particles on top of the ZnO array. The as fabricated chip is immersed in a 5 mM AgNO₃ solution (in DI water) and irradiated under a UV lamp (~30 W m⁻² intensity) for one hour. The finished chip was then washed with DI water to remove excess product and dried at room temperature. All reagents in the synthesis were purchased from Sigma Aldrich.

2.3 SEM and EDS characterization

The scanning electron microscopy (SEM) was performed on a FEI Helios 5CX dual beam scanning electron microscope operating at 5 kV. The energy-dispersive X-ray spectroscopic (EDS) measurements and the chemical mapping were performed with the SDD X-ray detector (Ametek®) attached to the TESCAN Vega3 scanning electron microscope operating at 30 kV.

2.4 Oxycodone detection using SERS measurement

The 1 mg mL⁻¹ oxycodone solution was diluted into 500 μg mL⁻¹, 10 μg mL⁻¹, 1 μg mL⁻¹, and 100 ng mL⁻¹ solutions. Each concentration had three replicates. Then ~5 μL of each sample was pipetted onto the prepared silver particles decorated ZnO



(Ag@ZnO) array substrates. A He-Ne laser beam (power = 10 mW, wavelength = 532 nm) was focused onto the substrate through a Raman spectrometer (Horiba labRAM Raman/AIST-NT AFM). The Raman signals of oxycodone were collected by an air-cooled open electrode 1024×256 pixel CCD detector. A standard silicon substrate was applied for calibration before all the measurements and its spectra was used for background correction. For the blood sample oxycodone detection test, de-identified patient serum samples were used, and they were obtained from Dartmouth-Hitchcock Medical Center (Lebanon, NH, USA). All samples were handled according to Dartmouth's Environmental Health and Safety and BSL-2 protocols. Blood serum sample were kept in a freezer before the test. The oxycodone solution was added to the raw blood serum that was diluted 100 times with phosphate buffered saline (PBS, Sigma Aldrich) in the serum samples to obtain $900 \mu\text{g mL}^{-1}$, $90 \mu\text{g mL}^{-1}$, $9 \mu\text{g mL}^{-1}$, 900 ng mL^{-1} and 90 ng mL^{-1} . For each concentration, measurements at 5 different locations selected randomly on the chip were carried out with point scan of the Raman spectroscopy. The Raman measurement and parameters are identical to the previous test.

3 Results and discussion

In this project, we designed and fabricated zinc oxide (ZnO) arrays on silicon (Si) wafers for the label-free and sensitive detection of opioids. ZnO has become popular in biosensor applications due to its excellent electrochemical and optoelectronic properties, low-cost manufacturing, versatility, and relative eco-friendliness. In this study, we fabricated silver (Ag) particles decorated ZnO arrays on silicon (Si) wafers and utilized them as portable, label-free, and efficient surface-enhanced

Raman spectroscopy (SERS)-based sensors. These chips were fabricated *via* a three-step fabrication process containing a ZnO seeding, hydrothermal growth of the vertically aligned ZnO array and a UV irradiation of the Ag particles. The summarized fabrication process and the schematic of the silver particles decorated ZnO array (Ag@ZnO) chip are depicted in Fig. 1. The ZnO array provides a 3 dimensional (3D) substrate for the Ag particles and the effectiveness of such 3D structure for SERS based sensing has been proven by previous works.^{47–49} The high electromagnetic enhancement factor induced by the 3D ZnO array structure mainly stems from the high surface area to volume ratio that allows for a much higher load of metal particles. Other advantages of ZnO arrays include their inability to absorb visible light, high controllability over size and dimensions, stability in regular environment, and suitability for mass production.⁴⁸ In addition, the enhancement effect may also be contributed by plasmonic resonance due to the coupling of the incident light to the surface plasmons enabled by the pathways formed in the small gaps between the ZnO rods.⁵⁰

The as-fabricated chip was then characterized by EDS (Fig. 2). Fig. 2A shows the top view of the chip where Ag particles are distributed on the top surface of the ZnO rods. Fig. 2B is a zoom-in image that shows the hexagonal cross section of a ZnO rod with Ag particles on the top surface. The Ag particles can also be seen on the side wall of ZnO rods as shown in Fig. 2C. From the SEM images, it is confirmed that Ag particles are placed on both the top surface and the side wall of the ZnO array. The average width of the cross section of the ZnO rod is approximately $2 \pm 0.3 \mu\text{m}$, and the size range of the Ag particles is approximately 50–200 nm in diameter. Fig. 2D shows the cross-section view of the chip, and the height is approximately

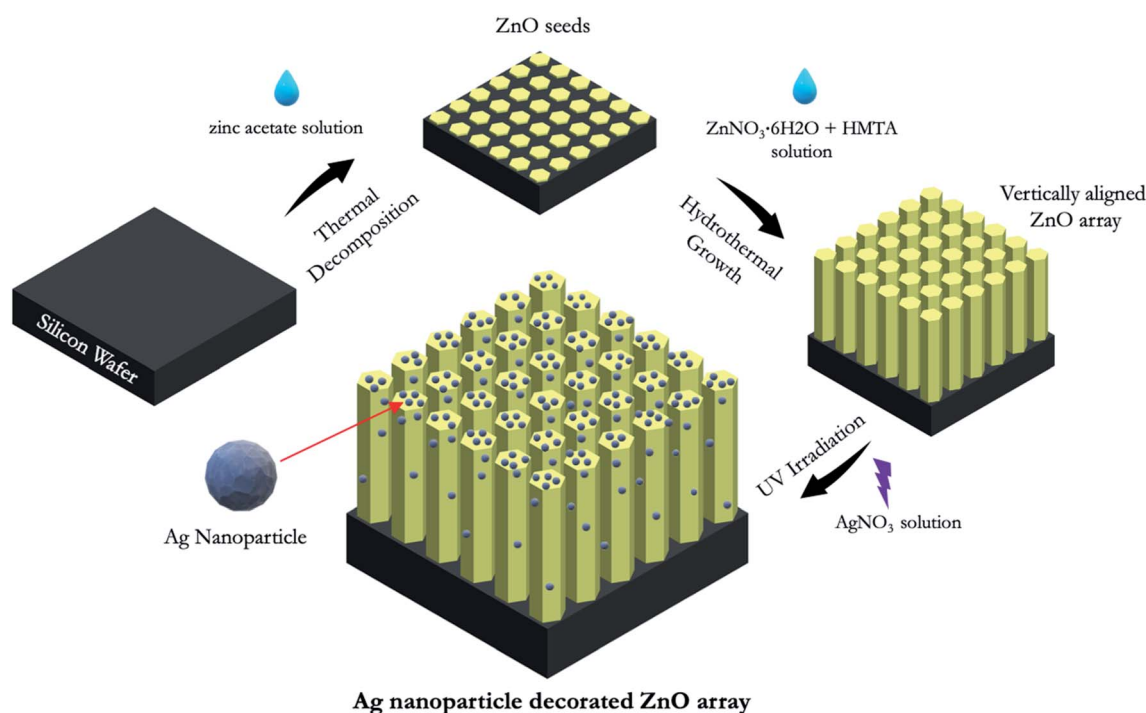


Fig. 1 Schematic of the Ag@ZnO chip and its fabrication process.



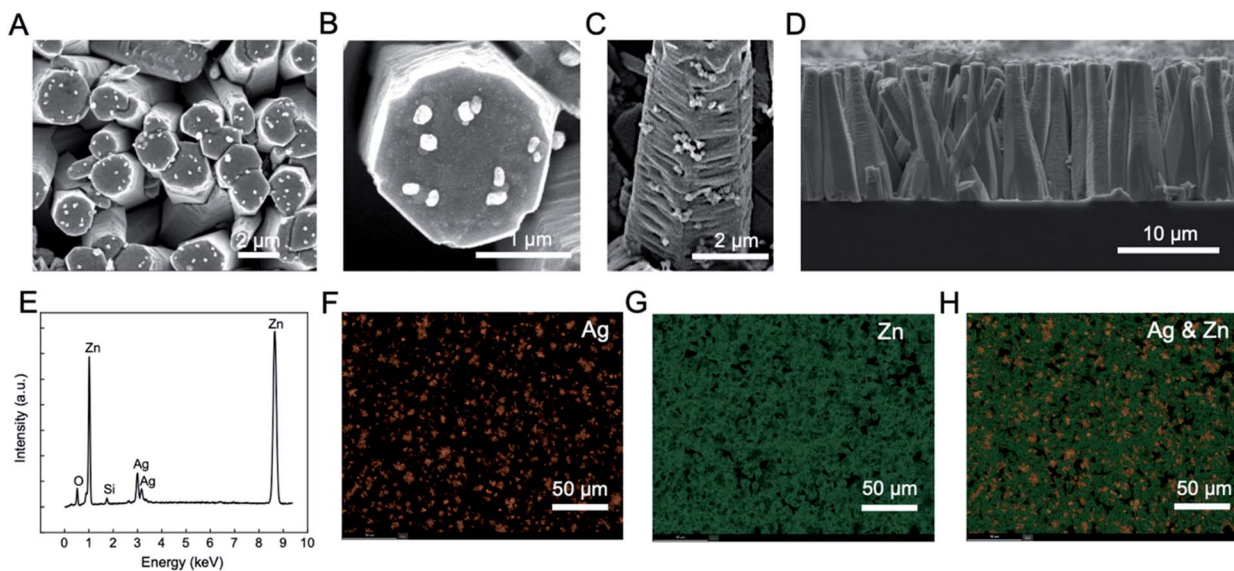


Fig. 2 Material characterization of the Ag@ZnO chip. (A) The SEM image of the top view of the chip. (B) A zoom-in image showing Ag particles on the top of a ZnO rod. (C) A zoom-in image showing Ag particles on the side wall of a ZnO rod. (D) The cross-section view showing the vertically aligned ZnO microarray. (E) The X-ray energy spectrum of the chip showing elements Zn, O, Ag and Si. (F) The EDS chemical mapping of the element Ag and (G) element Zn. (H) The combined EDS mapping of elements Ag and Zn confirming a relatively uniform dispersion of Ag particles on the ZnO microarray.

14 μm . The EDS spectrum confirming the existence of the element Ag, Zn, O and Si at their corresponding characteristic energy is shown in Fig. 2E. The Ag element has its characteristic energies at 2.98 and 3.15 keV; Zn element has the characteristic energy at 1.01 and 8.64 keV; O has its characteristic energy at 0.52 keV; Si's characteristic energy is at 1.74 keV. Fig. 2F and G are the chemical mapping of the element Ag and Zn, respectively. It is confirmed that the vertical ZnO rod and the Ag particles are uniformly distributed on the chip. In addition, Fig. 2H is the combined chemical mapping of both element Ag and Zn, indicating that the Ag particles are uniformly distributed on the ZnO array. The Ag particle content in terms of atomic ratio and weight ratio are 3.12% and 6.96%, respectively.

Prior to the experimental Raman tests, we simulated the localized surface plasmonic resonance effect using a simplified model using finite element method (FEM) in COMSOL. Fig. 3A shows the schematic of the simulation model. There are two scenarios of the particle placement. The first is a single Ag particle with 100 nm diameter that was positioned at the center of a ZnO plate. The second is a pair of Ag particles of the different sizes, *i.e.*, 50, 100 and 100 nm diameter, with an inter-particle distance of 50, 100 and 150 nm. We expected that a “hot spot” where a strong localized enhancement occur exists between two particles that are in a close proximity according to literature.^{34,35} The input excitation light was polarized along the long axis of the silver particle as shown in the figure and the electrical field was aligned with the two particles in the second scenario. Fig. 3B shows the plot of the extinction cross-sections area, *i.e.*, the sum of scattering and absorption cross-section area, of the silver particle at different wavelengths from 450 nm to 700 nm. The value of the extinction cross-section area reflects the local plasmonic enhancement effect of the particles.

In the simulation, there are three pairs of Ag particles that are 100 nm in diameter and with an inter-particle distance of 50, 100 and 150 nm. As shown in the plot, the peaks of the extinction cross-section area for all particle arrangements fall in the range of 500–550 nm (highlight by the grey area in Fig. 3B), which correspond to the localized plasmon resonance wavelength of these particle arrangements. It is shown that Ag particle pairs induce a greater extinction cross-section area across the entire wavelength range than a single Ag particle. This can be explained by the “hot spot” effect that is created between two Ag particles that are adjacent to each other with a short inter-particle distance. Fig. 3C shows the 2D and 3D simulation models of the localized surface plasmon enabled electrical field enhancement (indicated by the color contour) of the Ag particles decorated on a ZnO platform excited by a light of wavelength 540 nm. In this set of simulations, Ag particle pairs with 50, 100 and 150 nm particle diameter and 50, 100 and 150 nm inter-particle distance as well as a single particle of 100 nm diameter are tested. In Fig. 3C, when two Ag particles are closer to each other (*e.g.*, 50 nm separation), a “hot spot” will form in the gap between them, as indicated by the enhanced electrical field represented by the green, yellow and red color that bridging the two particles. On the other hand, as the particles moves farther apart from each other, as in the 100 and 150 nm separation case, the “hot spot” effect between them diminishes and vanishes eventually. Yet, the electromagnetic enhancement effect can also occur at a single Ag particle, as seen from all particle arrangements in the simulation, especially the single Ag particle one and the ones with the Ag particle pairs farther apart (*e.g.*, 150 nm inter-particle distance). Therefore, even individual Ag particles or ones that are very far apart from each other can have an increased local plasmonic effect as



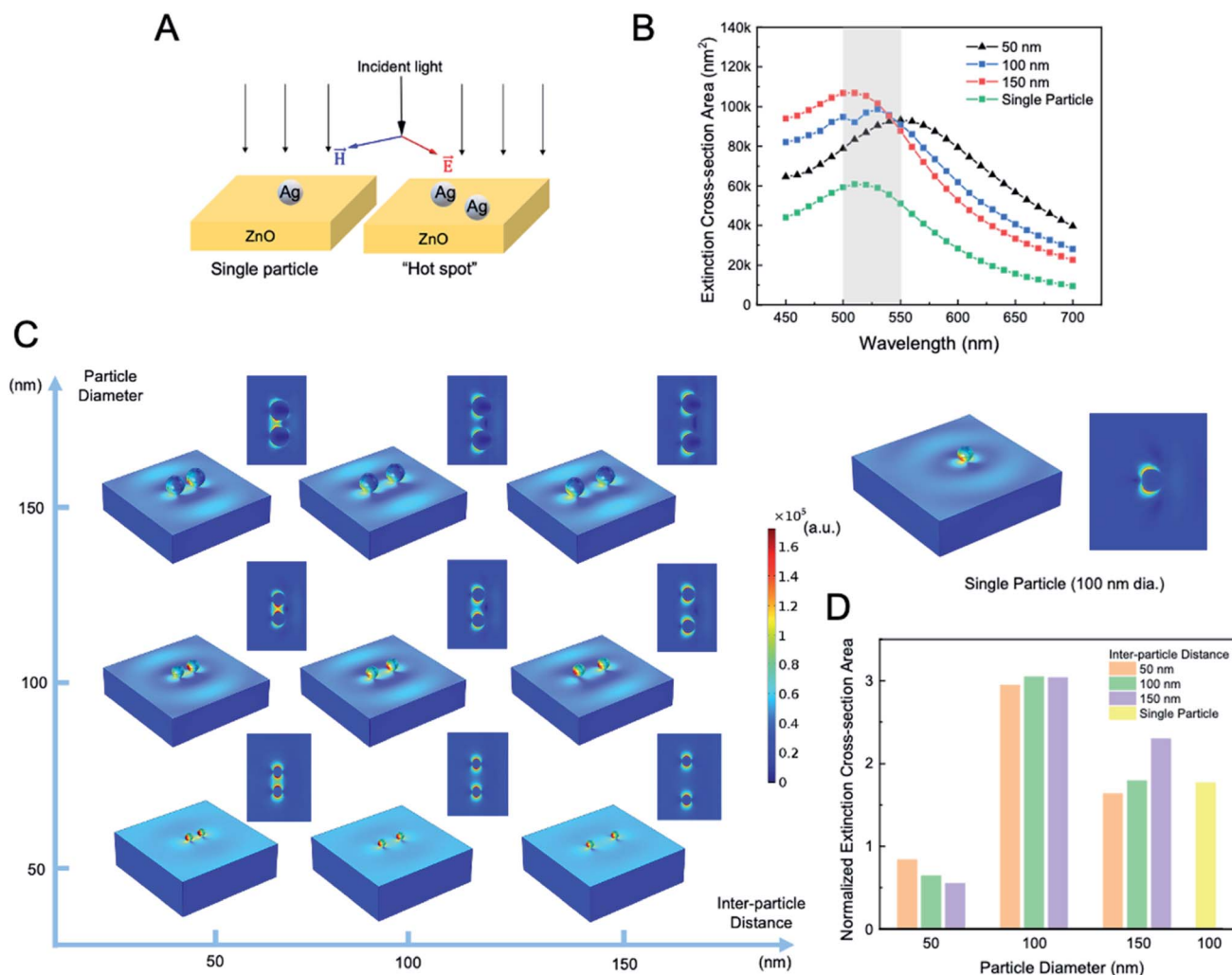


Fig. 3 Simulation of the localized surface plasmon enabled electrical field enhancement of the Ag particle decorated ZnO. (A) The schematic of the model including two scenarios: a single particle and a pair of particles close to each other. (B) The extinction cross-section area of the Ag particle(s) of 100 nm in diameter in a wavelength range from 450 nm to 700 nm. The grey area highlights the range of peaks of all particle arrangements. (C) The simulated 3D model and the cross-sectional mapping showing the electric intensity of the Ag particle(s) excited by a light of 540 nm wavelength. The color bar represents electric field intensity. (D) The normalized extinction cross-section area of the Ag particle pairs with 50, 100 and 150 nm diameters and with 50, 100 and 150 nm inter-particle distances and of a single Ag particle.

a result of coupling of electromagnetic of the Ag particle and the ZnO substrate. The plot in Fig. 3D quantitatively summarizes the simulation result. It is shown that the 100 nm diameter particles have the greatest normalized extinction cross-section area or greatest enhancement effect than the 50 and 150 nm diameter ones. Here, the normalized value is defined by the extinction cross-section area divided by the total surface area of the particles. In addition, for the 100 nm diameter cases, the particle pairs have a stronger enhancement effect than the single particle scenario. It is shown that at the resonance wavelength of 550 nm, the light excited local electric field has the greatest intensity compared to those of 470 and 650 nm wavelength. Further, we observed that the highest intensity occurs at the Ag–ZnO interface for all cases and at the side of the particles that is facing each other in two-particle cases from which a “hot spot” is created. Overall, the simulation results demonstrated that a “hot spot” can occur when two Ag particles are close to each other and that local

enhancement also occur between the Ag particle and the ZnO substrate. In either case, the Ag particle shows the greatest intensity of the light–matter interaction at its vicinity that can significantly enhance the Raman signal.

Next, in order to verify the viability of the chips' opioid sensing function, a quick test was performed on commercially available opioid-containing solutions before a more practical and systematic clinical study using human blood. Specifically, we tested our device using a solution containing oxycodone, a potent and commonly abused opioid, dissolved in methanol as a quick feasibility study. Opioid-containing solutions at varying concentrations were tested using the as-fabricated chip as a platform for label-free SERS-based detection of oxycodone whose chemical structure is shown in Fig. 4A. 5 μ L solutions containing oxycodone dissolved in methanol were dropped onto the chip placed under the objective lens of a Raman spectrometer, the substrate was exposed to a focused laser with



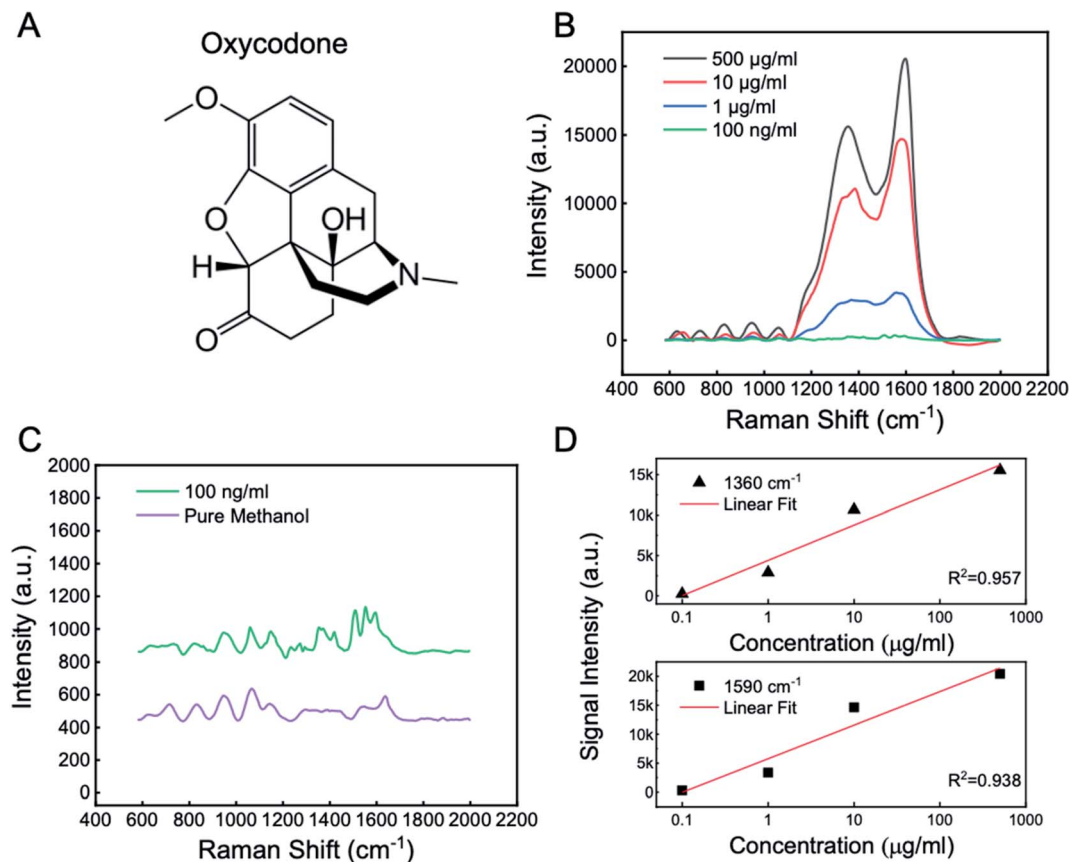


Fig. 4 Measured SERS signal for varying oxycodone concentrations. (A) The chemical structure of oxycodone. (B) The SERS signal from tested oxycodone solutions with oxycodone concentrations of $500 \mu\text{g mL}^{-1}$, $10 \mu\text{g mL}^{-1}$, $1 \mu\text{g mL}^{-1}$, and 100 ng mL^{-1} , and pure methanol with a common baseline. (C) Comparison of the SERS peaks of the 100 ng mL^{-1} oxycodone solution and the pure methanol. (D) The signal intensity of the Raman spectroscopy of the 1360 nm peak and the 1590 nm peak showing a near-linear relationship with the oxycodone concentration in the logarithmic scale plot.

a wavelength of 532 nm which is determined from the simulation that shows a resonance at $550\text{--}560 \text{ nm}$ where the simulated signal is at its highest level (Fig. 3B). Oxycodone concentrations of $500 \mu\text{g mL}^{-1}$, $10 \mu\text{g mL}^{-1}$, $1 \mu\text{g mL}^{-1}$ and 100 ng mL^{-1} showed the highest characteristic peaks in the Raman spectroscopy with a common baseline at around 1360 cm^{-1} and 1590 cm^{-1} (Fig. 4B) which agree with the recently reported values.^{51,52} The $\sim 1360 \text{ cm}^{-1}$ band is attributed to the stretching CC bond in ring C, the bending CH bond, and the wagging CH_2 bond in ring B, while the $\sim 1590 \text{ cm}^{-1}$ band is attributed to the stretching CC bond in ring C, the wagging CH_2 bond in ring B.⁵³ In addition, pure methanol was measured under the same test condition as a control group and showed no peaks at around 1360 cm^{-1} and 1590 cm^{-1} compared to the 100 ng mL^{-1} concentration of oxycodone as shown in Fig. 4C. Note that, for the 100 ng mL^{-1} oxycodone solution, although signal noise is present due to a low intensity of signal, the 1360 cm^{-1} and 1590 cm^{-1} peaks are still distinguishable. Furthermore, the signal intensity of the Raman spectroscopy for both peaks are plotted at each of the oxycodone concentration (Fig. 4D). It is shown that the Raman signal intensity increases as oxycodone concentration increases, and it is a near-linear relationship in the logarithmic scale plot as indicated by the linear fit curve

with an R^2 value being 0.957 and 0.938 for the 1360 cm^{-1} and 1590 cm^{-1} characteristic peaks, respectively. All these Raman curves for different concentrations share the same Raman shift locations for each of the corresponding peaks, proving the excellent repeatability of the test on the Ag@ZnO chip. From this test, it is demonstrated that the Ag@ZnO chips could provide a high-throughput method for mapping detailed patterns of oxycodone to a large range of concentration from $500 \mu\text{g mL}^{-1}$ to 100 ng mL^{-1} , thereby leading to the next more practical, clinical trial using human blood serum.

Lastly, after the viability of the chips' opioid sensing function was verified through a quick proof-of-concept test using commercially available opioid-containing solution, we performed a more practical clinical study using human blood serum samples. Specifically, we tested the Ag@ZnO array chip with serum samples containing oxycodone with five different concentrations, that is, $900 \mu\text{g mL}^{-1}$, $90 \mu\text{g mL}^{-1}$, $9 \mu\text{g mL}^{-1}$, 900 ng mL^{-1} and 90 ng mL^{-1} . The preparation of the serum sample and the experimental method are detailed in the Experimental section. Like the previous test, these samples were tested using the as-fabricated chip as a platform for label-free SERS-based technique, and the same Raman settings and parameters were used for this test. Fig. 5A–E show the Raman signal spectrum for



each oxycodone concentration of $900 \mu\text{g mL}^{-1}$, $90 \mu\text{g mL}^{-1}$, $9 \mu\text{g mL}^{-1}$, 900 ng mL^{-1} and 90 ng mL^{-1} , respectively. All spectrums show the highest characteristic peaks at around 1360 cm^{-1} and 1590 cm^{-1} which agree with the previous test (Fig. 4B) and recently reported values.^{51,52} Again, the $\sim 1360 \text{ cm}^{-1}$ band is attributed to the stretching C–C bond in ring C, the bending C–H bond, and the wagging $-\text{CH}_2$ bond in ring B, while the $\sim 1590 \text{ cm}^{-1}$ band is attributed to the stretching C–C bond in ring C, the wagging $-\text{CH}_2$ bond in ring B of the oxycodone molecule.⁵³ It is worth noting that even the lowest oxycodone concentration, 90 ng mL^{-1} , clearly shows the distinctive characteristic peaks, demonstrating a superb detection ability at his low concentration which is on the same level of the lowest concentration reported by literature using immunoassay and GC-MS method (*i.e.*, 10 ng mL^{-1}).^{4,54} Yet, compared with these two testing strategies, the testing method presented in this work

using SERS technique with the Ag@ZnO nanochip is less laborious, time-consuming, and expensive. From applying the serum sample to the chip to reading a reliable, meaningful result, it only takes less than 10 minutes. Further, the Raman signal from each oxycodone concentration is summarized in Fig. 5F with a common baseline for comparison purpose. All Raman spectrums share the same 1360 cm^{-1} and 1590 cm^{-1} characteristic peaks of oxycodone and their signal intensity decreases as the oxycodone concentration decreases. To show the relationship between the signal strength and the concentration, the intensity of the Raman spectroscopy of at 1360 cm^{-1} and 1590 cm^{-1} characteristic peaks are plotted at each of the oxycodone concentration (Fig. 5G and H). For both peaks, the Raman signal intensity increases as oxycodone concentration increases. The linear regression model shows a positive linear relationship between the oxycodone concentration and the

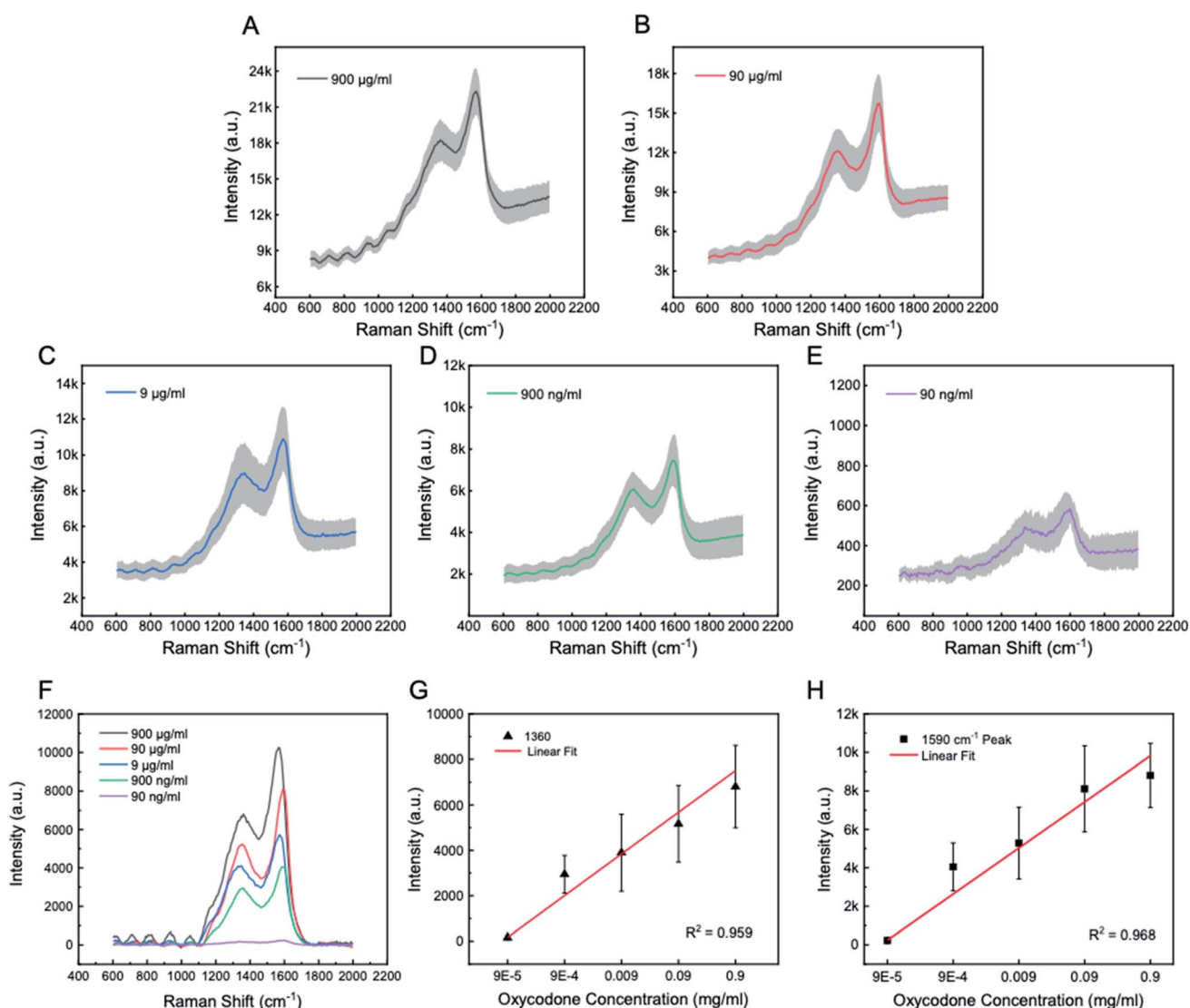


Fig. 5 SERS signals from five blood serum samples with different oxycodone concentrations. The individual SERS signal with oxycodone concentrations of (A) $900 \mu\text{g mL}^{-1}$, (B) $90 \mu\text{g mL}^{-1}$, (C) $9 \mu\text{g mL}^{-1}$, (D) 900 ng mL^{-1} and (E) 90 ng mL^{-1} with error bars (the shaded area). (F) Comparison of the SERS signals of all oxycodone concentrations with a common baseline. (G) The signal intensity versus oxycodone concentrations at the characteristic peaks at 1360 cm^{-1} and (H) 1590 cm^{-1} (error bars represent standard deviation of data points).



signal intensity (in the logarithmic scale plot) with an R^2 being 0.959 and 0.968 for the 1360 cm^{-1} and 1590 cm^{-1} characteristic peaks, respectively, exhibiting a good sensitivity of this detection technique. From this test with blood serum samples, it is demonstrated that the Ag@ZnO chips and the SERS technique provide a high-throughput method for detecting the opiate substance oxycodone by identifying its characteristic peaks for a large range of concentrations (from $900\text{ }\mu\text{g mL}^{-1}$ to 90 ng mL^{-1}) and with excellent accuracy and sensitivity.

The SERS based enhancement is attributed primarily to two underlying mechanisms, namely, the electromagnetic mechanism and the chemical mechanism. The former is associated with the localized surface plasmonic resonance and the resulted enhanced electric field and light–matter interaction. The latter is based on the resonance of the incident photon energy and charge transfers. The electromagnetic mechanism is the dominating mechanism as its enhancement is several orders of magnitude larger than that of the chemical mechanism.³³ Furthermore, in this work, there are a number of factors that determines the magnitude of the SERS enhancement including the intrinsic properties of the decorated Ag particles and ZnO, the size of the particles and the interparticle distance. The gap between two close Ag particles will create a “hot spots” which contribute to a significant SERS enhancement and it is believed that the shorter the interparticle distance, the larger the enhancement.³⁵ In addition, although the Ag particles are randomly distributed, their fabrication and deposition parameters (e.g., silver nitrate concentration, UV intensity, exposure time) can be precisely controlled so that the density and size of the particles can be finely designed. As a result, the variance between each as-fabricated substrate can be minimized to ensure reproducibility. Also, by using a filter of the Raman spectroscopy in the future that allows for higher power from the laser, we can expect enhanced signals and can find the detection limit of the concentration of oxycodone that is below 90 ng mL^{-1} .

4 Conclusion

We demonstrated a Ag decorated ZnO arrays chip, using a facile two-step fabrication strategy, for the SERS detection of opioids. Our results show that this design allows for a large SERS detection range for opioids concentrations, from $900\text{ }\mu\text{g mL}^{-1}$ to 90 ng mL^{-1} , with remarkable accuracy and sensibility. This is due to the plasmonic signal enhancement caused by the Ag particles scattered across a ZnO array scaffolding. We verified such amplification observed in experiments using the FEM simulation. Our detection method is label-free and portable, which holds great promise to be an effective point-of-care and solution for sensitive, high-throughput and low-cost drug abuse detection especially for opiate substances.

Author contributions

M. Z., C. J., and J. X. J. Z conceived the idea of detecting opioid substance using silver particle decorated ZnO array. M. Z. and C. J. contributed equally to this manuscript. M. Z. and C. J. designed and conducted the experiment and wrote the

manuscript. Y. N. conducted the Raman spectroscopy measurement. Y. R. performed the simulations. N. H. provided insightful ideas, important discussions and edited the manuscript. Z. X. and L. D. provided important discussions and edited the manuscript. J. X. J. Z. provided guidance, supervised the work and edited the manuscript.

Conflicts of interest

A United States patent application has been filed for the technology described in this work.

Acknowledgements

The authors acknowledge financial support from the National Institute of Health (NIH) Director's Transformative Research Award (R01HL137157, PI: X. J. Z.), the National Science Foundation award (ECCS1509369, PI: X. J. Z.), and the startup fund from the Thayer School of Engineering at Dartmouth. C. J. is thankful for the discussion and help of characterization from Dr Maxime Guinel in the EM facility at Dartmouth College.

References

- 1 H. Hedegaard, B. A. Bastian, J. P. Trinidad, M. Spencer and M. Warner, *Natl Vital Stat. Rep.*, 2018, **67**, 1–14.
- 2 B. Goldberger, C. Chronister and M. Merves, in *Clinical Applications of Mass Spectrometry*, ed. U. H.-S. Garg, Springer US, 2019, pp. 38–43.
- 3 J. L. Knittel, D. J. Clay, K. M. Bailey, M. A. Gebhardt and J. C. Kraner, *J. Anal. Toxicol.*, 2009, **33**, 433–438.
- 4 M. Gingras, M. H. Laberge and M. Lefebvre, *J. Anal. Toxicol.*, 2010, **34**, 78–83.
- 5 C. A. Haller, J. Stone, V. Burke, J. Branch, K. Chen and S. Gross, *J. Anal. Toxicol.*, 2006, **30**, 106–111.
- 6 A. Haddad, M. A. Comanescu, O. Green, T. A. Kubic and J. R. Lombardi, *Anal. Chem.*, 2018, **90**, 12678–12685.
- 7 M. M. Kimani, A. Lanzarotta and J. S. Batson, *J. Forensic Sci.*, 2020, 1–14.
- 8 A. Lanzarotta, M. Witkowski and J. C. Batson, *J. Forensic Sci.*, 2020, **65**, 421–427.
- 9 A. N. Masterson, S. Hati, G. Ren, T. Liyanage, N. E. Manicke, J. V Goodpaster and R. Sardar, *Anal. Chem.*, 2021, **93**, 2578–2588.
- 10 R. Mirsafavi, M. Moskovits and C. Meinhardt, *Analyst*, 2020, **145**, 3440–3446.
- 11 R. Salemmilani, M. Moskovits and C. D. Meinhardt, *Analyst*, 2019, **144**, 3080–3087.
- 12 C. Shende, A. Farquharson, C. Brouillette, W. Smith and S. Farquharson, *Molecules*, 2019, **24**, 2578.
- 13 C. Shende, C. Brouillette and S. Farquharson, *Analyst*, 2019, **144**, 5449–5454.
- 14 N. G. Wilson, J. Raveendran and A. Docoslis, *Sens. Actuators, B*, 2021, **330**, 129303.
- 15 V. Turzhitsky, L. Zhang, G. L. Horowitz, E. Vitkin, U. Khan, Y. Zakharov, L. Qiu, I. Itzkan and L. T. Perelman, *Small*, 2018, **14**, 1802392.



- 16 S. Pang, T. Yang and L. He, *TrAC, Trends Anal. Chem.*, 2016, **85**, 73–82.
- 17 R. Pilot, R. Signorini, C. Durante, L. Orian, M. Bhamidipati and L. Fabris, *Biosensors*, 2019, **9**, 57.
- 18 L. Bao, S. Han, X. Sha, H. Zhao, Y. Liu, D. Lin and W. Hasi, *J. Spectrosc.*, 2019, **2019**, 1–5.
- 19 Y. Shan, Y. Yang, Y. Cao, C. Fu and Z. Huang, *Nanotechnology*, 2016, **27**, 145502.
- 20 K. A. Willets and R. P. Van Duyne, *Annu. Rev. Phys. Chem.*, 2007, **58**, 267–297.
- 21 G. Barbillon, V. E. Sandana, C. Humbert, B. Bélier, D. J. Rogers, F. H. Teherani, P. Bove, R. McClintock and M. Razeghi, *J. Mater. Chem. C*, 2017, **5**, 3528–3535.
- 22 Y. F. Chan, H. J. Xu, L. Cao, Y. Tang, D. Y. Li and X. M. Sun, *J. Appl. Phys.*, 2012, **111**, 033104.
- 23 L. Chen, L. Luo, Z. Chen, M. Zhang, J. A. Zapien, C. S. Lee and S. T. Lee, *J. Phys. Chem. C*, 2010, **114**, 93–100.
- 24 H. Yadav, N. Sinha, S. Goel and B. Kumar, *J. Alloys Compd.*, 2016, **689**, 333–341.
- 25 G. Sinha, L. E. Depero and I. Alessandri, *ACS Appl. Mater. Interfaces*, 2011, **3**, 2557–2563.
- 26 L. M. Chen and Y. N. Liu, *ACS Appl. Mater. Interfaces*, 2011, **3**, 3091–3096.
- 27 G. Shan, S. Zheng, S. Chen, Y. Chen and Y. Liu, *Colloids Surf., B*, 2012, **94**, 157–162.
- 28 K. Sivashanmugan, J. Der Liao, B. H. Liu, C. K. Yao and S. C. Luo, *Sens. Actuators, B*, 2015, **207**, 430–436.
- 29 W. Song, X. Han, L. Chen, Y. Yang, B. Tang, W. Ji, W. Ruan, W. Xu, B. Zhao and Y. Ozaki, *J. Raman Spectrosc.*, 2010, **41**, 907–913.
- 30 Y. Xie, S. Yang, Z. Mao, P. Li, C. Zhao, Z. Cohick, P. H. Huang and T. J. Huang, *ACS Nano*, 2014, **8**, 12175–12184.
- 31 Y. Zang, J. Yin, X. He, C. Yue, Z. Wu, J. Li and J. Kang, *J. Mater. Chem. A*, 2014, **2**, 7747–7753.
- 32 C. Cheng, B. Yan, S. M. Wong, X. Li, W. Zhou, T. Yu, Z. Shen, H. Yu and H. J. Fan, *ACS Appl. Mater. Interfaces*, 2010, **2**, 1824–1828.
- 33 H. Hu, Z. Wang, S. Wang, F. Zhang, S. Zhao and S. Zhu, *J. Alloys Compd.*, 2011, **509**, 2016–2020.
- 34 J. Huang, F. Chen, Q. Zhang, Y. Zhan, D. Ma, K. Xu and Y. Zhao, *ACS Appl. Mater. Interfaces*, 2015, **7**, 5725–5735.
- 35 A. E. Kandjani, M. Mohammad Taheri, A. Thakkar, S. K. Bhargava and V. Bansal, *J. Colloid Interface Sci.*, 2014, **436**, 251–257.
- 36 A. E. Kandjani, Y. M. Sabri, M. Mohammad-Taheri, V. Bansal and S. K. Bhargava, *Environ. Sci. Technol.*, 2015, **49**, 1578–1584.
- 37 S. Lei, C. Tao, J. Li, X. Zhao and W. Wang, *Appl. Surf. Sci.*, 2018, **452**, 148–154.
- 38 F. Li, S. Wu, L. Zhang and Z. Li, *J. Mater. Sci.: Mater. Electron.*, 2017, **28**, 16233–16238.
- 39 H. H. Park, X. Zhang, K. W. Lee, A. Sohn, D. W. Kim, J. Kim, J. W. Song, Y. S. Choi, H. K. Lee, S. H. Jung, I. G. Lee, Y. D. Cho, H. B. Shin, H. K. Sung, K. H. Park, H. K. Kang, W. K. Park and H. H. Park, *Nanoscale*, 2015, **7**, 20717–20724.
- 40 Y. Tan, J. Gu, W. Xu, Z. Chen, D. Liu, Q. Liu and D. Zhang, *ACS Appl. Mater. Interfaces*, 2013, **5**, 9878–9882.
- 41 Q. Li, Y. Jiang, R. Han, X. Zhong, S. Liu, Z. Y. Li, Y. Sha and D. Xu, *Small*, 2013, **9**, 927–932.
- 42 T. T. Nhung, Y. Bu and S. W. Lee, *J. Cryst. Growth*, 2013, **373**, 132–137.
- 43 N. Hao, Z. Xu, Y. Nie, C. Jin, A. B. Closson, M. Zhang and J. X. J. Zhang, *Chem. Eng. J.*, 2019, **378**, 122222.
- 44 C. Jin, N. Hao, Z. Xu, I. Trase, Y. Nie, L. Dong, A. Closson, Z. Chen and J. X. J. Zhang, *Sens. Actuators, A*, 2020, **305**, 111912.
- 45 C. Xu, P. Shin, L. Cao and D. Gao, *J. Phys. Chem. C*, 2009, **114**, 125–129.
- 46 L. Wang, D. Tsan, B. Stoeber and K. Walus, *Adv. Mater.*, 2012, **24**, 3999–4004.
- 47 S. Li, N. Zhang, N. Zhang, D. Lin, X. Hu and X. Yang, *Sens. Actuators, B*, 2020, **321**, 128519.
- 48 S. Picciolini, N. Castagnetti, R. Vanna, D. Mehn, M. Bedoni, F. Gramatica, M. Villani, D. Calestani, M. Pavesi, L. Lazzarini, A. Zappettini and C. Morasso, *RSC Adv.*, 2015, **5**, 93644–93651.
- 49 C. Huang, C. Xu, J. Lu, Z. Li and Z. Tian, *Appl. Surf. Sci.*, 2016, **365**, 291–295.
- 50 M.-K. Nguyen, W.-N. Su and B.-J. Hwang, *Adv. Healthcare Mater.*, 2017, **6**, 1601290.
- 51 S. Farquharson, C. Brouillette, W. Smith and C. Shende, *Front. Chem.*, 2019, **7**, 1–16.
- 52 S. Farquharson, C. Shende, A. Sengupta, H. Huang and F. Inscore, *Pharmaceutics*, 2011, **3**, 425–439.
- 53 V. Rana, M. V. Cañamares, T. Kubic, M. Leona and J. R. Lombardi, *J. Forensic Sci.*, 2011, **56**, 200–207.
- 54 R. Meatherall, *J. Anal. Toxicol.*, 2005, **29**, 301–308.

